Next Materials 9 (2025) 101202

Contents lists available at ScienceDirect

Next Materials

journal homepage: www.sciencedirect.com/journal/next-materials

Research article

Revisiting the Li–Na system: Ab initio based description of the low-temperature thermodynamics for battery applications

Lara Caroline Pereira dos Santos [a,*], Markus Mann [b], Christian Schwab [b], Dina Fattakhova-Rohlfing [b], Martin Finsterbusch [b], Robert Spatschek [a,c]

[a] Institute of Energy Materials and Devices IMD-1, Forschungszentrum Jülich GmbH, Jülich, 52425, NRW, Germany
[b] Institute of Energy Materials and Devices IMD-2, Forschungszentrum Jülich GmbH, Jülich, 52425, NRW, Germany
[c] JARA-ENERGY, Jülich, 52425, NRW, Germany

ARTICLE INFO

Keywords:
Thermodynamics
Ab initio
First-principles
Lithium
Sodium
Metal anode
Solid state batteries

ABSTRACT

We revisit the thermodynamics of the Li–Na system below the eutectic temperature (≈ 350 K), where both elements tend to form essentially immiscible bcc phases. Ab initio calculations are used to extract the energetics and to optimize the non-ideal interaction terms of the Gibbs energy, especially in the dilute limit. The obtained optimized description is used to predict the low-temperature (below 350 K) metallic phase diagram and the spinodal regime. Furthermore, elastic coherency effects are included. The resulting descriptions are used to interpret and predict the microstructure formation in Li–Na metal anodes for all-solid state batteries, providing a theoretical composition range where such microstructure is expected to form.

1. Introduction

Lithium is one of the key elements for the ongoing energy transition, as it enables the storage of renewable energy to replace fossil sources. This is particularly crucial for automotive applications, where developing active battery materials with high energy density, cycle stability and low cost is decisive. Currently, the most used anode concept for Li-ion batteries is based on graphite. But the hope is that in the future all-solid-state batteries will allow to use lithium directly as anode material to maximize the energy density. However, it turns out that even in such setups the use of pure Li as anode material could lead to undesired effects, such as the formation of dendrites [1]. A possible mitigation strategy is to alloy it with low amounts of other elements, which can improve the overall behavior. Among these, sodium has emerged as a promising candidate [2–5]. Specifically, a recent study has highlighted the low-temperature phase formation of Li–Na metal anodes, which shows potential to deliver enhanced electrochemical performance in all-solid-state batteries [4].

Li–Na, as a binary system, has been previously investigated, with its phase diagram detailed in [7], building upon earlier descriptions in [8]. These authors have developed a comprehensive thermodynamic modeling, based on existing experimental work and the SGTE data [9], leading in particular to the phase diagram shown in Fig. 1. Li–Na is a monotectic alloy, hence it exhibits phase separation in the melt phase [10]. Additionally, it has a lower temperature eutectic point on the Na rich side. It is therefore obvious that the focus of these investigations was on the high temperature regime of the phase diagram, to capture the behavior in the vicinity of these invariant points [11–19]. In contrast, less attention has been paid to the low-temperature regime below the eutectic temperature (≈350 K), where Li and Na form essentially immiscible body-centered cubic (bcc) phases.

Therefore, in this paper, we revisit the low-temperature regime of the Li–Na phase diagram, using ab initio techniques, as these low solubility regimes are difficult to access experimentally. Based on these investigations, we suggest an improved thermodynamic description of the bcc phases at low temperatures. Apart from phase stability, also spinodal decomposition is investigated, as it is considered to be relevant for the Li–Na anodes. In addition, this chemical perspective is extended by the consideration of isotropic elastic effects, to estimate the role of internal mechanical strains on the phase stability and spinodal decomposition. The consequences of the new assessment are discussed from the perspective of battery applications, and used to interpret and predict the microstructure formation in Li–Na metal anodes, as well as providing a theoretical composition range where such microstructure is expected to form.

2. Methods

All ab initio simulations are performed with the Vienna Ab initio Simulation Package (VASP), which uses a plane wave basis set and the

* Corresponding author.
E-mail address: l.pereira.dos.santos@fz-juelich.de (L.C.P. dos Santos).

https://doi.org/10.1016/j.nxmate.2025.101202
Received 2 September 2025; Received in revised form 5 September 2025; Accepted 8 September 2025
Available online 16 September 2025

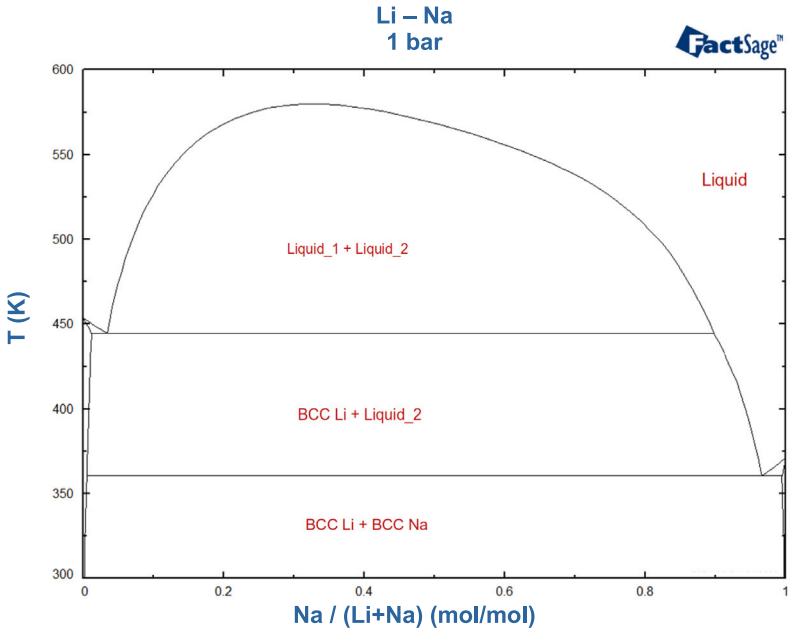

Fig. 1. Li–Na equilibrium phase diagram, adapted from the SGTE database in FactSage 8.3 and [6]. At around 75 K lithium undergoes a phase transition towards a dense packed structure, which is shown in [6], but not depicted and not relevant here.

projector augmented wave (PAW) method [20–22]. Different supercell sizes ranging from $2 \times 2 \times 2$ to $4 \times 4 \times 4$ are used, where one or more Na atoms replace Li atoms on the bcc positions. A full ionic relaxation is performed with an energy accuracy of 10^{-5} eV in between two ionic steps. The electronic self-consistency loop has a global break condition of 10^{-6} eV. The exchange–correlation energy is determined via the Perdew–Burke–Ernzerhof (PBE) generalized gradient approximation (GGA) using the harder pseudopotentials that include the valence states *s* for Li and *p* for Na [23]. An energy cutoff for the plane-wave basis set of 500 eV and a $10 \times 10 \times 10$ Monkhorst–Pack k-point mesh are selected for the simulations [24].

3. Results and discussions

3.1. Low-temperature thermodynamics

For the application as anode material, mainly the low-temperature phases of Li–Na are of interest. As obvious from the phase diagram, the mutual solubility of Na in Li and vice versa is rather low. Consequently, data on this regime is limited, and the thermodynamic modeling in [7] has presumably only reduced accuracy. Therefore, we perform ab initio calculations at 0 K to obtain the energetics of the Li–Na system.

The results of the density functional theory computations are summarized in Fig. 2. It shows the energy of formation (per atom), using the definition

$$E_f(N_{\mathrm{Li}}, N_{\mathrm{Na}}) = E(N_{\mathrm{Li}}, N_{\mathrm{Na}}) - N\left[(1-x)E_{\mathrm{Li}} + xE_{\mathrm{Na}}\right], \tag{1}$$

where $N = N_{\mathrm{Li}} + N_{\mathrm{Na}}$ is the total number of atoms in the substitutional alloy, in analogy to the definition in [25]. Here, $E(N_{\mathrm{Li}}, N_{\mathrm{Na}})$ denotes the energy of a system consisting of N_{Li} lithium and N_{Na} sodium atoms, and $E_{\mathrm{Li}} = E(N, 0)/N$ is the energy per (pure) lithium atom (similarly $E_{\mathrm{Na}} = E(0, N)/N$). Furthermore, $x = N_{\mathrm{Na}}/N$ is the sodium concentration. By definition, the energy of formation difference equals zero for both pure Li and pure Na. Alloys which contain both elements have a higher formation energy E_f, indicating that at $T = 0$ K no solid solution phase is formed, and instead a decomposition into pure Li and pure Na takes place, which is in agreement with the experimental phase diagram. Eq. (1) can be interpreted as total energy of the system, from which a linear function in concentration is subtracted. Such a subtraction affects neither the common tangent construction for identifying phase coexistence nor the condition for the onset of spinodal decomposition, which will be discussed below.

Due to the equivalence of bcc lattice positions, the energy is unique for setups with only a single impurity. For two such defects, the energy depends on their relative position, which leads to a slight scatter in the data. This effect is most pronounced for an equal amount of Li and Na atoms ($x = 0.5$), where the highest energy configurations correspond to irregular "solid solution" configurations, whereas the lower ones to arrangements, where the different atom types are organized in layers or blocks. This energy reduction relative to the solid solution configurations indicated the system's tendency for phase separation. As we treat the phase separation on the continuum level, we mainly focus here on the randomly arranged high energy configurations; further improvements using special quasirandom structures are possible [26]. However, we point out that the focus of the present investigations is on solubility limits and spinodal decomposition, which occur at low concentrations. Therefore, only these unique branches at $x \approx 0$ and $x \approx 1$ are relevant and considered for the determination of an optimized thermodynamic description in the following. Moreover, in the present investigations, only $T = 0$ K energies from the ab initio simulations are used. For higher temperatures closer to the eutectic temperature, next to configurational entropy contribution, which are discussed below, also thermal vibrations should be considered. The focus of the present work is formally on low-temperature phase separation, where vibrational modes are not yet excited. Especially on the Li rich side, such an approximation is reasonable due to the higher Debye temperature of Li as compared to Na [27]. This simplification is in line with existing thermodynamic descriptions, but an extension to quasiharmonic descriptions is possible, similar to discussions in, e.g., [28].

Finite temperature configurational entropy is added via the ideal solution model, in agreement with the Calphad description. We note that not all lattice configurations are energetically equivalent, thus the use of the ideal model, which assumes equal probability for all states, is strictly speaking not appropriate. However, as we are here mainly interested in the low-concentration regimes, only small amounts of Na in the bcc Li lattice (and vice versa) are relevant. As all lattice positions in the bcc lattice are equivalent, as discussed above, and the distance

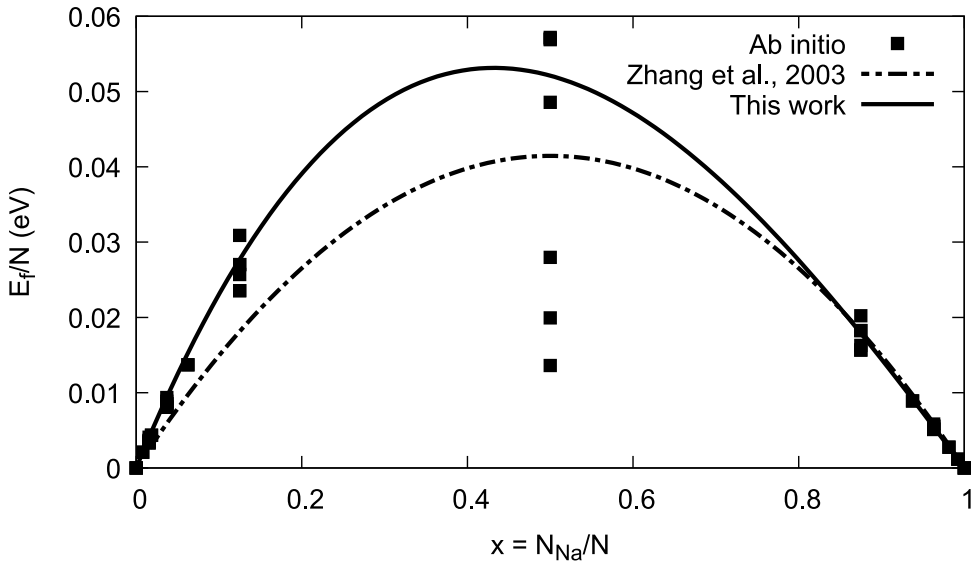

Fig. 2. Ab initio based formation energy of the Li–Na system. The low energy configurations in $x = 0.5$ correspond to partially ordered structures, where Li and Na are arranged in layers, in agreement with the energy reduction through phase separation.

between Na atoms is large for low concentrations, the assumption is appropriate. For higher concentrations, deviations are captured in the Calphad framework in the excess Gibbs energy expression, as defined below.

From a thermodynamics perspective, the finite temperature Gibbs energy is modeled as

$$G_{\mathrm{m}}^{\Phi} = \sum_i x_i {}^0G_i^{\Phi} + RT\sum_i x_i \ln x_i + {}^{\mathrm{xs}}G_{\mathrm{m}}^{\Phi} \tag{2}$$

within the Calphad framework. Here, the molar Gibbs energies ${}^0G_i^{\Phi}$ of the pure element i with structure Φ as described in [9], and R is the ideal gas constant, in agreement with the usual normalization as Gibbs energy per mole. The non-ideal, excess contribution is expressed through the Redlich–Kister polynomials as

$${}^{\mathrm{xs}}G_{\mathrm{m}}^{\Phi} = \sum_i \sum_{j>i} x_i x_j \sum_{k=0}^{n} {}^kL_{i,j}^{\Phi}(x_i - x_j)^k. \tag{3}$$

Zhang et al. [7] truncates the expansion after the leading term for the bcc Li–Na phase, using ${}^0L_{\mathrm{Li,Na}}^{\mathrm{bcc}} = 16000\,\mathrm{J/mol}$. For $T = 0\,\mathrm{K}$ the excess contribution ${}^{\mathrm{xs}}G_{\mathrm{m}}^{\Phi}$ corresponds to the formation energy E_f (apart from the normalization per mole), i.e. ${}^{\mathrm{xs}}G_{\mathrm{m}}^{\Phi} = N_A E_f/N$, and the expression from [7] is depicted in Fig. 2. Although the agreement with the ab initio data is reasonable, it does not capture well the apparent asymmetry between the Li and Na rich sides. Therefore, we suggest to include also the next order term in the Redlich–Kister expansion. This leads to an improved description in the low-temperature and low-concentration regime. At elevated temperatures, also temperature dependent Redlich–Kister coefficients would be required, which is beyond the scope of the present article.

Consequently, an analysis of the low-concentration and low-temperature regime of the common tangent construction yields for the solubility limit of Na in Li

$$x \simeq \exp\left(-\frac{{}^{\mathrm{xs}}G_{\mathrm{m}}^{\Phi\prime}(x=0)}{RT}\right), \tag{4}$$

where the prime denotes differentiation with respect to the Na concentration x, see [29]. On the Na rich side, one gets similarly

$$1 - x \simeq \exp\left(\frac{{}^{\mathrm{xs}}G_{\mathrm{m}}^{\Phi\prime}(x=1)}{RT}\right). \tag{5}$$

An expansion up the second term in Eq. (3) yields on the Li rich side

$$x \simeq \exp\left(-\frac{{}^0L_{\mathrm{Li,Na}}^{\mathrm{bcc}} + {}^1L_{\mathrm{Li,Na}}^{\mathrm{bcc}}}{RT}\right) \tag{6}$$

and similarly on the Na rich side

$$1 - x \simeq \exp\left(-\frac{{}^0L_{\mathrm{Li,Na}}^{\mathrm{bcc}} - {}^1L_{\mathrm{Li,Na}}^{\mathrm{bcc}}}{RT}\right). \tag{7}$$

These expressions show that for a description of the low-concentration regimes the coefficients ${}^0L_{\mathrm{Li,Na}}^{\mathrm{bcc}}$ and ${}^1L_{\mathrm{Li,Na}}^{\mathrm{bcc}}$, as well as the solubility limits, are directly related to the slope of the ab initio computed formation energy at $x = 0$ and $x = 1$. As the computed energies with one Na or Li defect are unique, the coefficients therefore follow directly from a finite difference expression,

$${}^0L_{\mathrm{Li,Na}}^{\mathrm{bcc}} + {}^1L_{\mathrm{Li,Na}}^{\mathrm{bcc}} = N_A\Big[E(N-1;1) - (N-1)E_{\mathrm{Li}} - E_{\mathrm{Na}}\Big], \tag{8}$$

$${}^0L_{\mathrm{Li,Na}}^{\mathrm{bcc}} - {}^1L_{\mathrm{Li,Na}}^{\mathrm{bcc}} = N_A\Big[E(1;N-1) - (N-1)E_{\mathrm{Na}} - E_{\mathrm{Li}}\Big], \tag{9}$$

using here the results from the largest calculated $4 \times 4 \times 4$ system, which contains $N = 128$ atoms. Solving the above linear system yields ${}^0L_{\mathrm{Li,Na}}^{\mathrm{bcc}} = 20109.8\,\mathrm{J/mol}$ and ${}^1L_{\mathrm{Li,Na}}^{\mathrm{bcc}} = 5772.6\,\mathrm{J/mol}$, leading to the new formation energy curve shown in Fig. 2, which agrees well with the ab initio data also in the intermediate concentration regime.

Figs. 3 and 4 show the low-temperature solubility limits both on the Li and Na rich side in an Arrhenius representation. Obviously, the exact expressions, as obtained from the common tangent construction, agree well with the low-temperature asymptotics (6) and (7). The graphs also contain the predictions from the previous assessment [7]. Whereas on the Na rich the two descriptions lead to very similar results, the new assessment leads to a significantly lower solubility limit on the Li rich side. We note that the phase equilibrium between the two bcc phases plays a role only below the eutectic temperature $T_e \approx 370\,\mathrm{K}$.

Beyond the thermodynamic phase stability we can also use the description to evaluate the onset of spinodal decomposition. The spinodal regime is in between the inflection points of the Gibbs energy curve, $G_{\mathrm{m}}^{\Phi\prime\prime}(x) = 0$. Apart from a numerical solution of this condition, also analytical approximations in the low-concentration regime (either $x \ll 1$ or $1 - x \ll 1$) can be worked out easily. For the Li rich side, we can neglect the configurational term $(1-x)\ln(1-x)$, and then the condition for the inflection point becomes approximately

$$x_{\mathrm{spin}} \approx -\frac{RT}{{}^{\mathrm{xs}}G_{\mathrm{m}}^{\Phi\prime\prime}(x=0)} = \frac{RT}{2\times{}^0L_{\mathrm{Li,Na}}^{\mathrm{bcc}} + 6\times{}^1L_{\mathrm{Li,Na}}^{\mathrm{bcc}}}, \tag{10}$$

hence the onset of spinodal decomposition increases linearly with temperature. An analogous analysis on the Na rich side yields

$$1 - x_{\mathrm{spin}} \approx -\frac{RT}{{}^{\mathrm{xs}}G_{\mathrm{m}}^{\Phi\prime\prime}(x=1)}$$

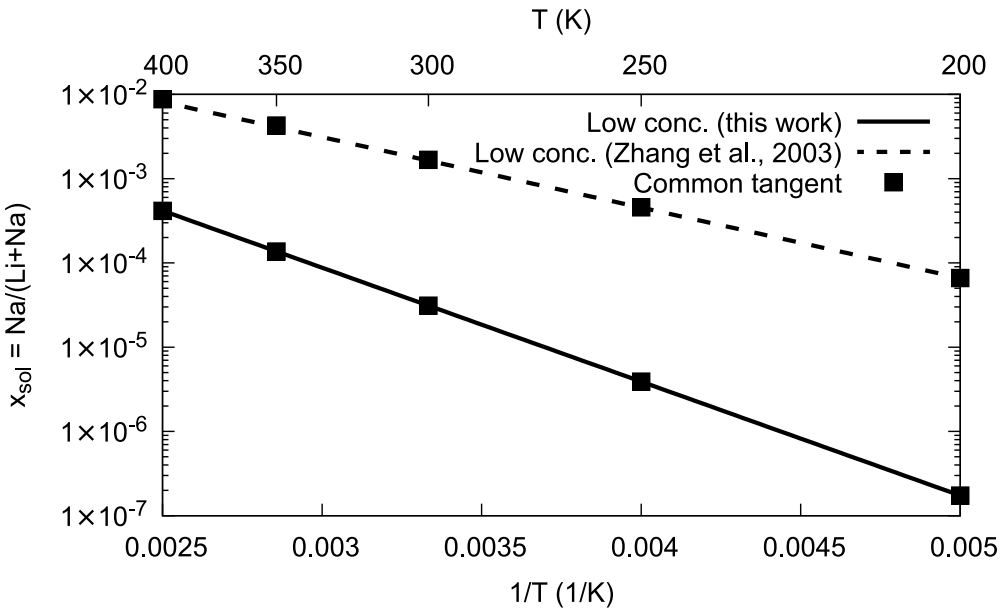

Fig. 3. Na solubility limit in Li in an Arrhenius representation, i.e. the Li rich side of the Li–Na phase diagram. The straight lines result from the low-concentration limit (6) for both the assessment by Zhang et al. [7] and the present work. They agree well with the full common tangent construction (squares) for each description in the entire temperature regime.

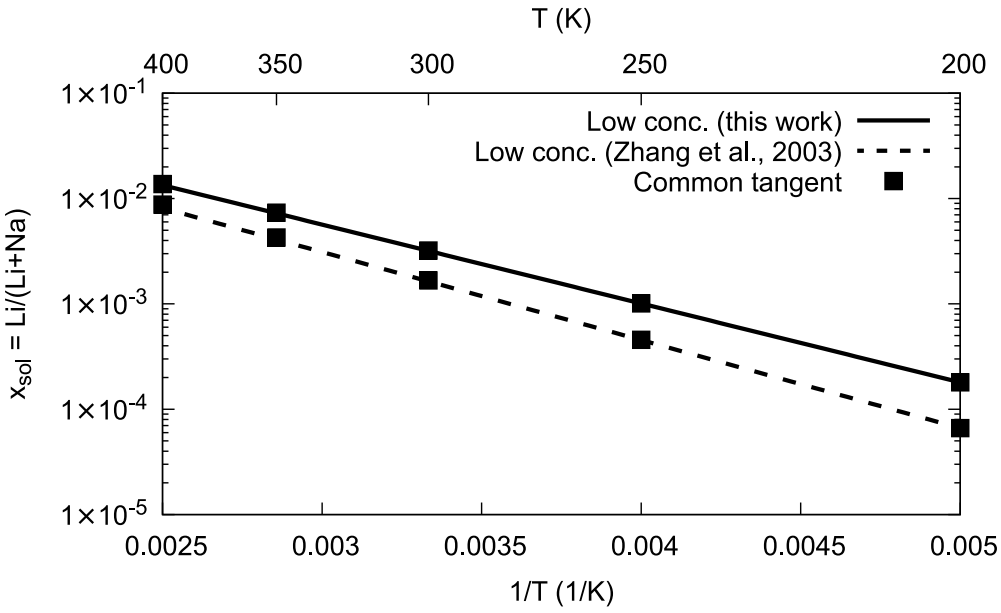

Fig. 4. Li solubility limit in Na in an Arrhenius representation, i.e. the Na rich side of the Li–Na phase diagram. The straight lines result from the low-concentration limit (7) for both the assessment by Zhang et al. [7] and the present work. They agree well with the full common tangent construction (squares) for each description in the entire temperature regime.

$$= \frac{RT}{2\times {}^{0}L^{\mathrm{bcc}}_{\mathrm{Li,Na}} - 6\times {}^{1}L^{\mathrm{bcc}}_{\mathrm{Li,Na}}}. \tag{11}$$

Fig. 5 compares the analytical approximations (10) and (11) to the numerically determined onset of spinodal decomposition. Especially on the Li rich side that agreement is excellent, as the required concentrations for spinodal decomposition are still small. Nevertheless, the difference between the present and the previous description [7] is significant, since the old description leads roughly to twice as high critical concentration of Na to trigger spinodal decomposition. On the Na rich side, the analytical approximation (11) delivers reliable estimates only at very low temperatures, as at around 50 K the spinodal concentration is already high. This invalidates the assumptions used for the derivation of Eq. (11), which can therefore serve only as an order of magnitude estimate.

3.2. Elastic effects

The considerations so far neglect elastic effects, as usually done for thermodynamic descriptions. This assumes that in case of phase separation the two phases are separated such that they cannot deform each other. In many applications, however, the phases stick together, and if then different lattice constants emerge, they mutually deform one another, which leads to an additional elastic energy contribution. This contribution always makes the phase separation less favorable, as

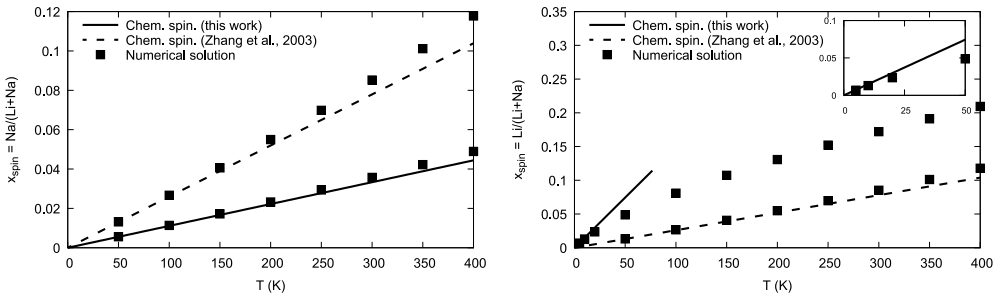

Fig. 5. Left panel: Begin of the spinodal regime on the Li rich side. Right panel: End of the spinodal regime on the Na rich side. The plots compare for both the previous assessment [7] and the present description the analytical approximation (10) to the exact numerical solution (black squares). On the Na rich side, the inset refers to the low-concentration regime of the chemical spinodal curve as obtained from our analytical model and numerical solutions. The expansion is valid only at low concentrations, as shown in this inset magnification.

in a single phase material without external mechanical constraints all macroscopic stresses can relax.

At this point, it is instructive to compare the above ab initio predictions to simulations without ionic relaxation, where all atoms are forced to remain on the equilibrium positions of the pure Li lattice. As sodium has a larger equilibrium lattice constant than lithium, this leads to compressed states if Li is replaced by Na. From the computed energies we then get a negative formation energy, which indicates that in this case no phase separation would occur and instead a solid solution should form. This improper prediction is a consequence of the artificially strong internal elastic deformations, which make the phase separation energetically unfavorable, as the emerging sodium phase is strongly compressed. However, from this result we conclude that elastic effects can have a substantial influence on phase coexistence in Li–Na.

A more realistic description is based on the assumption of coherent precipitation of the second phase. In contrast to the above perspective, elastic relaxation is permitted, such that the total elastic energy, which arises due to lattice mismatches, is minimized. This perspective gives an upper bound to the influence of elastic effects, as additional relaxation effects, e.g., due to plasticity, creep or interface slip are not considered. Therefore, we follow a similar approach as in [30,31], where mechanical effects are taken into account using a mean field description. Such approaches are further elaborated and justified in [29], also with the extension towards the inclusion of elastic relaxation near free surfaces [32]. The calculation is based on the assumption of forming coherent interfaces between the emerging phases and linear elasticity. Further major assumptions are the isotropy of the elastic constants and the lattice expansion through the increase of the sodium concentration. In this case, the Bitter-Crum theorem [33] applies in infinite or periodic systems, and therefore the elastic energy becomes a function of the volume fractions of the two involved phases alone and does not depend on their spatial arrangement. As suggested by Cahn [34], the elastic effects can effectively be described by adding an elastic contribution (with dimension energy per mole)

$$G_{\mathrm{el}} = \frac{E\chi^2\Omega_0 N_A}{N_0(1-\nu)}x^2 \tag{12}$$

to the existing description. An explicit proof for this result is given in [29]. In the above expression, E is Young's modulus, ν the Poisson ratio, χ the Vegard coefficient of lattice expansion, Ω_0 the volume of a unit cell and N_0 the number of atoms per unit cell. It is assumed that both phases have the same elastic constants, and that they differ only by a concentration dependent isotropic eigenstrain $\epsilon_{ij}^{(0)} = \delta_{ij}\chi x$. With pure lithium as reference phase we use $\Omega_0 = a_{\mathrm{Li},0}^3$ with $a_{\mathrm{Li},0} = 3.42$ Å being the $T = 0$ K lattice constant of bcc Li and $N_0 = 2$ for a bcc lattice. The Vegard coefficient is approximated as $\chi = (a_{\mathrm{Na},0} - a_{\mathrm{Li},0})/a_{\mathrm{Li},0}$, using $a_{\mathrm{Na},0} = 4.19$ Å. The values of the elastic constants of Li and Na and their anisotropy will be discussed in detail elsewhere. Here, we use as upper bound Young's modulus of lithium in isotropic approximation as $E = 13.8$ GPa and a Poisson ratio of $\nu = 0.33$.

As derived in detail in [29] an analogous low-temperature Arrhenius behavior can be obtained from the generalized common tangent construction, which reads on the Li rich side

$$x \simeq \exp\left(-\frac{{}^{\mathrm{xs}}G_{\mathrm{m}}^{\Phi\prime}(x=0) + \Delta G_{\mathrm{el}}}{RT}\right) \tag{13}$$

with

$$\Delta G_{\mathrm{el}} = -\frac{E\chi^2\Omega_0 N_A}{N_0(1-\nu)}. \tag{14}$$

An analogous description can be obtained for the Na rich side. Results for the low-concentration regime for the coherent binodals both for the description [7] and the present one are shown in Fig. 6. As expected, the coherent phase separation can occur only inside the chemical binodal regime, hence elastic effects increase the solubility limits. The reason is that elastic coherency contributions appear only in two phase configurations, which are therefore energetically less favorable. Although mechanical anisotropy and contrast of elastic constants formally lead to deviations from the above mean field results, the solubility limits will only weakly be affected by these corrections.

Similar to the above approach, also the coherent spinodals can be calculated [34], which is done for simplicity using the assumption of elastic isotropy again. The consideration of cubic elasticity on coherent spinodal decomposition has been elaborated in [35], and has only minor influence on the predicted stability limits here. Also, the concentration dependence of the elastic constants leads only to higher order corrections. It turns out that the description based on [7] leads to a critical temperature around 205 K, which is significantly below the eutectic temperature, contrary to the new assessment. Here, one has to keep in mind that rather an upper bound for the elastic effects has been calculated. Also, the non-ideal Gibbs energy contribution (3) is optimized to deliver reliable predictions in the dilute regime, and therefore the behavior near a possible critical point may not be captured well.

Altogether, all results can be combined, leading to the new phase diagram below the eutectic temperature, see Fig. 7. The coherent phase diagram becomes very asymmetric, whereas the previous description leads to a symmetric phase diagram. Compared to the previous description, the Na solubility limit in Li is therefore reduced, whereas more Li is soluble in Na.

3.3. Relevance for Li–Na anodes

Enabling lithium metal as electrode in all-solid-state batteries is a key step for enhanced energy density and safety. However, it is frequently reported that the limited self diffusion of Li and the morphological instability of the lithium metal anode restrict the rate capability of these cells. During lithium stripping, pore formation takes place at the interface due to the slow diffusion kinetics of vacancies in the lithium metal, see, e.g., [36]. These authors report that alloying with

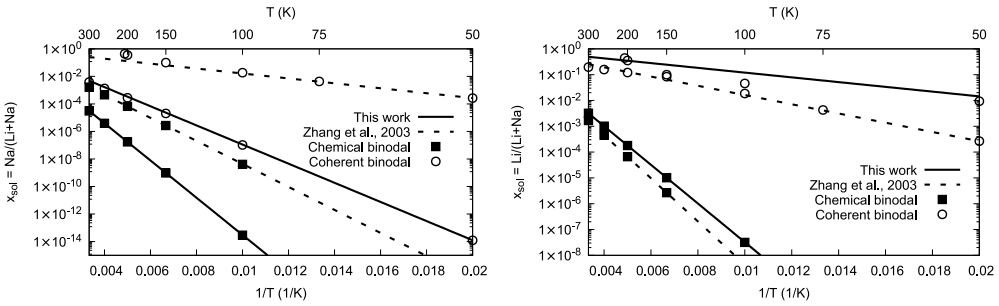

Fig. 6. Chemical and coherent binodals, calculated both with the previous model [7] and the present description. Left panel: Li rich side. Right panel: Na rich side. The solid straight lines correspond to the new description, the dashed lines to [7], using the low-concentration approximations. The exact solutions from the common tangent constructions are shown as symbols, where the squares correspond to the chemical binodal (without elastic effects), and the open circles to the coherent binodals. Notice that for the coherent binodals at higher temperatures the circles deviate slightly from the exponential asymptotic approximations.

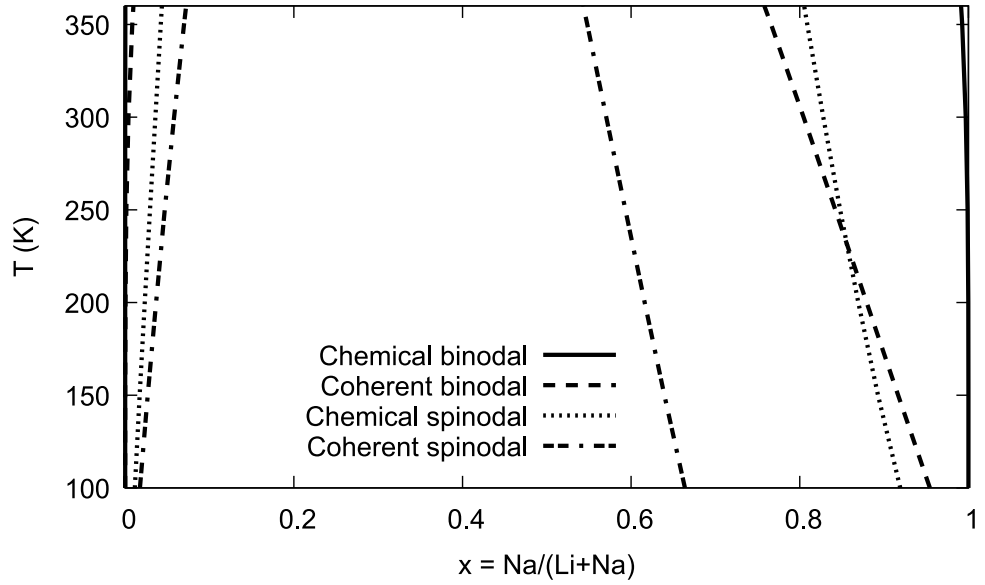

Fig. 7. Phase diagram of the Li–Na system up to the eutectic temperature, according to the ab initio based description in this work. In particular on the Li rich side, the solubility limit is very low, hence the chemical binodal appears on this scale as a vertical line.

Mg leads to stable solid solution phases which can stabilize the interface and lead to better performance.

Recently, a complementary approach was presented, which is based on the mechanical mixing with small amounts of sodium to lithium [4]. This approach differs strongly from the Mg alloying, as Li–Na are essentially immiscible at low temperatures, as discussed in the preceding sections. Therefore, phase separation is an immediate consequence from equilibrium thermodynamics. However, by alloying Li with 3 at% Na via mechanical mixing, heating above the melting point and quenching to room temperature sufficiently fast, a metastable solid solution or finely dispersed structures emerge. Only during a formation step at the first cycles a scaffold structure establishes, consisting of Li and Na rich regions, which form a complex three-dimensional network with characteristic pattern scale of the order 10 µm (see Fig. 8, which is reused from [4] and licensed under CC BY 4.0). As there were no indications for the formation of such a microstructure already from the liquid state during quenching, the question of a possible mechanism for the origin of this pattern arises through a solid-state phenomenon. During the initial formation step, the Li concentration in the anode is reduced during stripping, and therefore the alloy is quenched isothermally deeper into the two phase region. An appealing mechanism for the emergence of a Na rich phase would be by nucleation and growth. Nonetheless, inspection of the microstructure indicates that the scaffold structures are spatially rather uniform, whereas nucleation as a thermally activated random event and subsequent fast growth would rather suggest the emergence of irregular structures. Instead, the scaffold structure shows similarities to evolving structures from spinodal decomposition, which raises the question whether this barrierless transformation process may at least initiate or support the scaffold formation.

Due to the small amount of Na, the low-temperature eutectic point on the sodium rich side is only indirectly relevant, whereas the monotectic point on the Li rich side turns out to be an important feature for composition and process design. In a first step, Li and Na at the monotectic composition are mechanically mixed at room temperature. This mechanical mixing, which can be handled in advance in the sense of a industrial processing, is mainly intended as a pre-mixing step, whereas direct alloying would lead to immediate phase separation, which turns out to be less suitable [3]. Then, the temperature of the assembled symmetrical cell is raised above the monotectic temperature, such that a homogeneous Li–Na melt phase can form. Due to the mechanical mixing, the required holding time for this homogenization is rather short. With the chosen composition, the melting temperature is minimized, and similarly it is avoided to bring the alloy neither into the low-concentration miscibility gap nor into the range of the monotectic demixing. As in both cases phase separation involving at least one liquid phase with fast diffusion would result, rather rapid microstructure formation would take place, e.g., by monotectic solidification [37]. This would be detrimental for the anode performance, and is indeed not observed [4]. We can indirectly conclude that through the

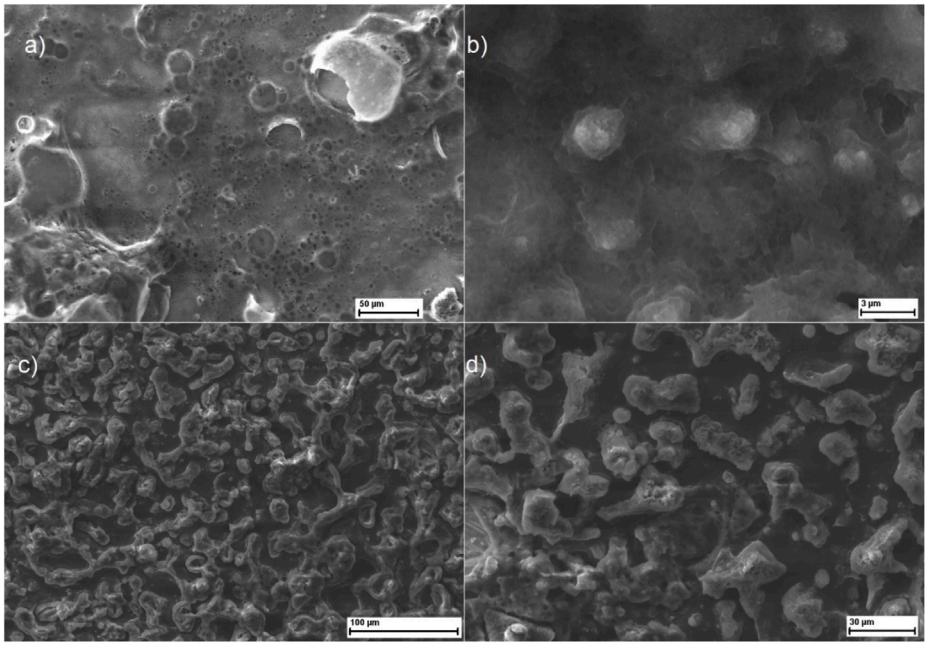

Fig. 8. SEM images at different magnifications of the remaining sodium structure after complete lithium stripping of one side of a symmetrical half-cell with Li–Na anodes and LLZO separators. (a, b): LLZO surface, while (c, d): Ni current collector surface. Images reused from [4] and licensed under CC BY 4.0.

choice of the monotectic composition and sufficiently fast quenching, the alloy is maintained in a metastable state with at most nanoscale sized precipitates.

This perspective is plausible from the description developed in the previous sections. Although at room temperature the solubility limit of Na (chemical binodal) is only around $x \approx 3 \cdot 10^{-5}$ and therefore below the nominal composition of 3 at%, spinodal decomposition sets in at around 3.6 at%. Coherency effects can further stabilize the metastable solid solution to a solubility limit of $x \approx 3.8 \cdot 10^{-3}$ with coherent spinodal decomposition starting at 5.8 at%. During the formation step of the symmetric Li–Na/LLZO/Li–Na cell the sodium concentration is increased due to stripping of lithium, and the alloy definitely enters the spinodal regime, which can trigger the observed scaffold formation. Moreover, inside the electrode a concentration gradient emerges during stripping of lithium due to the finite diffusivity of Li. This explains the observation in Fig. 8 that the Li–Na/LLZO interface consists essentially of Na only, as the lithium is depleted there. In contrast, the Li–Na alloy remains in the solid solution regime for a longer time near the current collector before phase separation is triggered, and therefore there a finer scaffold structure is observed.

We point out that spinodal decomposition alone will presumably not be able to entirely explain the scaffold formation due to kinetic reasons. The kinetics of this process are usually described by the Cahn-Hilliard equation, which is a fourth order equation, and is directly related to the original discrete treatment by Hillert [38]. It describes the initial rapid development of concentration fluctuations and the following phase separation into essentially depleted local equilibrium phases. After this initial growth regime, coarsening is driven by the reduction of interfacial energy. Quantitatively, the coarsening regime was investigated in [39]. The authors show that for a phase independent kinetic coefficient the coarsening is in line with classical Ostwald ripening [40,41]. Hence, it shows a scaling of the characteristic length scale of the patterns as $R \sim (d_0 Dt)^{1/3}$, as for interface controlled diffusion, the scaling obeys $R \sim t^{1/4}$. Using characteristic values for Li and Na diffusion coefficients, which are of the order $\sim 10^{-10}\,\mathrm{cm}^2/\mathrm{s}$ in the relevant temperature regime (from room temperature to ~60 °C; the ionic conductivity is typically too low below these temperatures for battery applications) and a capillary length d_0, which is typically on atomic scales, it leads even after extended times to patterns which are on the submicron scale and thus below the scaffold pattern size experimentally observed [4]. Consequently, we believe that an additional acceleration through the ionic transport during stripping will ultimately form these structures, which are possibly initiated by the spinodal instability. In turn, the slow curvature driven coarsening in absence of electrical fields implies that the self-organized scaffold structure is rather robust against curvature driven coarsening even on extended lifetimes of batteries.

4. Conclusions

We have calculated the phase stability of bcc Li and Na in the low-temperature regime, where both elements show only low mutual solubility. By performing ab initio simulations to calculate the formation energy, which is used together with a configurational entropy expression for predicting the low-temperature phase coexistence, we revisit the Li–Na phase diagram and improve the current description. An asymmetry in the non-ideal interaction term calls for the inclusion of higher order terms in the Redlich–Kister expansion, therefore extending the work from [7]. Based on the new thermodynamics, we find a reduced solubility limit of Na in Li, compared to the previous study, which is in line with a theoretical Arrhenius description. Beyond phase stability, we also considered spinodal decomposition, which is expected to start at 3.6 at% at room temperature. The inclusion of mechanical coherency stresses rises the Na solubility limit and pushes the onset of coherent spinodal decomposition to higher Na concentrations (up to 5.8 at%). For all-solid-state batteries, we suggest that spinodal decomposition triggers the formation of a scaffold microstructure in Li–Na anodes during Li stripping, when the Na content is effectively increased. However, spinodal decomposition alone will not fully explain the microstructure formation due to sluggish coarsening kinetics.

Declaration of competing interest

The authors declare that they have no known competing financial interests or personal relationships that could have appeared to influence the work reported in this paper.

Acknowledgments

This work was funded by the German Federal Ministry of Education and Research (BMBF) via the project ALANO (grant no. 13XP0396B) and the Helmholtz project ZeDaBase. Open access was funded by the Deutsche Forschungsgemeinschaft (DFG, German Research Foundation) - 491111487. The authors gratefully acknowledge the computing time granted by the JARA Vergabegremium and provided on the JARA Partition part of the supercomputer JURECA at Forschungszentrum Jülich [42].

References

[1] N. Boaretto, I. Garbayo, S. Valiyaveettil-SobhanRaj, A. Quintela, C. Li, M. Casas-Cabanas, F. Aguesse, Lithium solid-state batteries: State-of-the-art and challenges for materials, interfaces and processing, J. Power Sources 502 (2021) 229919, http://dx.doi.org/10.1016/j.jpowsour.2021.229919.

[2] X. Fu, T. Wang, W. Shen, M. Jiang, Y. Wang, Q. Dai, D. Wang, Z. Qiu, Y. Zhang, K. Deng, Q. Zeng, N. Zhao, X. Guo, Z. Liu, J. Liu, Z. Peng, A high-performance carbonate-free Lithium|Garnet interface enabled by a trace amount of sodium, Adv. Mater. 32 (2020) http://dx.doi.org/10.1002/adma.202000575.

[3] Y. Zhang, J. Meng, K. Chen, H. Wu, J. Hu, C. Li, Garnet-based solid-state lithium fluoride conversion batteries benefiting from eutectic interlayer of superior wettability, ACS Energy Lett. 5 (4) (2020) 1167–1176, http://dx.doi.org/10.1021/acsenergylett.0c00383.

[4] M. Mann, C. Schwab, L.C.P. dos Santos, R. Spatschek, D. Fattakhova-Rohlfing, M. Finsterbusch, Improving the rate performance of lithium metal anodes: In-situ formation of 3D interface structures by mechanical mixing with sodium metal, Energy Storage Mater. 74 (2025) 103975, http://dx.doi.org/10.1016/j.ensm.2024.103975.

[5] S.G. Yoon, B.S. Vishnugopi, D.L. Nelson, A.X.B. Yong, Y. Wang, S.E. Sandoval, T.A. Thomas, K.A. Cavallaro, P. Shevchenko, E.P. Alsaç, C. Wang, A. Singla, J.R. Greer, E. Ertekin, P.P. Mukherjee, M.T. McDowell, Interface morphogenesis with a deformable secondary phase in solid-state lithium batteries, Sci. 388 (6751) (2025) 1062–1068, http://dx.doi.org/10.1126/science.adt5229.

[6] C.W. Bale, E. Bélisle, P. Chartrand, S.A. Decterov, G. Eriksson, A.E. Gheribi, K. Hack, I.-H. Jung, Y.-B. Kang, J. Melançon, A.D. Pelton, S. Petersen, C. Robelin, J. Sangster, P. Spencer, M.-A. Van Ende, FactSage thermochemical software and databases, 2010–2016, Calphad 54 (2016) 35–53, http://dx.doi.org/10.1016/j.calphad.2016.05.002.

[7] S. Zhang, D. Shin, Z. Liu, Thermodynamic modeling of the Ca–Li–Na system, Calphad 27 (2) (2003) 235–241, http://dx.doi.org/10.1016/j.calphad.2003.09.001.

[8] A.D. Pelton, Calculation of phase equilibria and thermodynamic properties of the Li-Na-H system, Int. J. Mater. Res. 84 (11) (1993) 767–772, http://dx.doi.org/10.1515/ijmr-1993-841107.

[9] A.T. Dinsdale, SGTE data for pure elements, Calphad 15 (4) (1991) 317–425, http://dx.doi.org/10.1016/0364-5916(91)90030-N.

[10] F.C. Campbell, Phase Diagrams: Understanding the Basics, ASM international, 2012.

[11] H.K. Schürmann, R.D. Parks, Paraconductivity in binary metallic liquids above the critical point, Phys. Rev. Lett. 27 (26) (1971) 1790, http://dx.doi.org/10.1103/PhysRevLett.27.1790.

[12] P.D. Feitsma, J.J. Hallers, F.V.D. Werff, W. Van der Lugt, Electrical resistivities and phase separation of liquid lithium-sodium alloys, Phys. B+C 79 (1) (1975) 35–52, http://dx.doi.org/10.1016/0378-4363(75)90105-9.

[13] M.G. Down, P. Hubberstey, R.J. Pulham, Sodium–lithium phase diagram: redetermination of the liquid immiscibility system by resistance measurement, J. Chem. Soc. (1975) 1490–1492, http://dx.doi.org/10.1039/DT9750001490.

[14] M.G. Down, P. Hubberstey, R.J. Pulham, Electrical resistivity of liquid sodium + lithium mixtures. Evidence for incipient immiscibility? J. Chem. Soc. Faraday Trans. 71 (1975) 1387–1391, http://dx.doi.org/10.1039/F19757101387.

[15] H. Endo, H. Hoshino, K. Tamura, M. Mushiage, Phase separation of liquid binary mixtures containing metals under pressure, Solid State Commun. 32 (12) (1979) 1243–1246, http://dx.doi.org/10.1016/0038-1098(79)90876-7.

[16] F.A. Kanda, R.C. Faxon, D.V. Keller, The determination of the liquid immiscibility boundaries of the lithium-sodium and thallium-selenium systems by the liquid density method, Phys. Chem. Liq. 1 (1) (1968) 61–72, http://dx.doi.org/10.1080/00319106808083787.

[17] E.S. Wu, H. Brumberger, Critical small-angle X-ray scattering of the liquid sodium-lithium system, Phys. Lett. A 53 (6) (1975) 475–477, http://dx.doi.org/10.1016/0375-9601(75)90674-X.

[18] W.H. Howland, L.F. Epstein, The binary system sodium-lithium, in: Handling and Uses of the Alkali Metals, American Chemical Society, 1957, pp. 34–41, http://dx.doi.org/10.1021/ba-1957-0019.ch005.

[19] O.N. Salmon, D.H. Ahmann, The lithiuim–sodium liquid metal system, J. Phys. Chem. 60 (1956) 13–16, http://dx.doi.org/10.1021/j150535a004.

[20] G. Kresse, J. Furthmüller, Efficient iterative schemes for ab initio total-energy calculations using a plane-wave basis set, Phys. Rev. B 54 (1996) 11169–11186, http://dx.doi.org/10.1103/PhysRevB.54.11169.

[21] P.E. Blöchl, Projector augmented-wave method, Phys. Rev. B 50 (1994) 17953–17979, http://dx.doi.org/10.1103/PhysRevB.50.17953.

[22] G. Kresse, D. Joubert, From ultrasoft pseudopotentials to the projector augmented-wave method, Phys. Rev. B 59 (1999) 1758–1775, http://dx.doi.org/10.1103/PhysRevB.59.1758.

[23] J.P. Perdew, K. Burke, M. Ernzerhof, Generalized gradient approximation made simple, Phys. Rev. Lett. 77 (1996) 3865–3868, http://dx.doi.org/10.1103/PhysRevLett.77.3865.

[24] H.J. Monkhorst, J.D. Pack, Special points for Brillouin-zone integrations, Phys. Rev. B 13 (1976) 5188–5192, http://dx.doi.org/10.1103/PhysRevB.13.5188.

[25] P.H. Mayrhofer, D. Music, J.M. Schneider, Ab initio calculated binodal and spinodal of cubic Ti1-xAlxN, Appl. Phys. Lett. 88 (7) (2006) 071922, http://dx.doi.org/10.1063/1.2177630.

[26] A. Zunger, S.-H. Wei, L.G. Ferreira, J.E. Bernard, Special quasirandom structures, Phys. Rev. Lett. 65 (1990) 353–356, http://dx.doi.org/10.1103/PhysRevLett.65.353.

[27] N.D. Tripathi, S.K. Pandey, Study of the effective debye temperature in alkali metals and their halides, Acust. 35 (1976) 278–280.

[28] B. Grabowski, T. Hickel, J. Neugebauer, Ab initio study of the thermodynamic properties of nonmagnetic elementary fcc metals: Exchange-correlation-related error bars and chemical trends, Phys. Rev. B 76 (2007) 024309, http://dx.doi.org/10.1103/PhysRevB.76.024309.

[29] R. Spatschek, G. Gobbi, C. Hüter, A. Chakrabarty, U. Aydin, S. Brinckmann, J. Neugebauer, Scale bridging description of coherent phase equilibria in the presence of surfaces and interfaces, Phys. Rev. B 94 (2016) 134106, http://dx.doi.org/10.1103/PhysRevB.94.134106.

[30] P.H. Mayrhofer, F.D. Fischer, H.J. Böhm, C. Mitterer, J.M. Schneider, Energetic balance and kinetics for the decomposition of supersaturated Ti1-xAlxN, Acta Mater. 55 (4) (2007) 1441–1446, http://dx.doi.org/10.1016/j.actamat.2006.09.045.

[31] P.H. Mayrhofer, L. Hultman, J.M. Schneider, P. Staron, H. Clemens, Spinodal decomposition of cubic Ti1-xAlxN: Comparison between experiments and modeling, Int. J. Mater. Res. 98 (11) (2007) 1054–1059, http://dx.doi.org/10.3139/146.101570.

[32] J. Weissmüller, Coherent phase change in interstitial solutions: A hierarchy of instabilities, Adv. Sci. 11 (21) (2024) 2308554, http://dx.doi.org/10.1002/advs.202308554.

[33] P. Fratzl, O. Penrose, J. Lebowitz, Modeling of phase separation in alloys with coherent elastic misfit, J. Stat. Phys. 95 (1999) 1429–1503, http://dx.doi.org/10.1023/A:1004587425006.

[34] J.W. Cahn, Coherent fluctuations and nucleation in isotropic solids, Acta Metall. 10 (1962) 907.

[35] J.W. Cahn, On spinodal decomposition in cubic crystals, Acta Metall. 10 (3) (1962) 179–183, http://dx.doi.org/10.1016/0001-6160(62)90114-1.

[36] T. Krauskopf, B. Mogwitz, C. Rosenbach, W.G. Zeier, J. Janek, Diffusion limitation of lithium metal and Li–Mg alloy anodes on LLZO type solid electrolytes as a function of temperature and pressure, Adv. Energy Mater. 9 (44) (2019) 1902568, http://dx.doi.org/10.1002/aenm.201902568.

[37] C. Hüter, G. Boussinot, E.A. Brener, R. Spatschek, Solidification in syntectic and monotectic systems, Phys. Rev. E 86 (2012) 021603, http://dx.doi.org/10.1103/PhysRevE.86.021603.

[38] M. Hillert, A solid-solution model for inhomogeneous systems, Acta Metall. 9 (6) (1961) 525–535, http://dx.doi.org/10.1016/0001-6160(61)90155-9.

[39] J. Zhu, L. Chen, J. Shen, V. Tikare, Coarsening kinetics from a variable-mobility Cahn-Hilliard equation: Application of a semi-implicit Fourier spectral method, Phys. Rev. E 60 (1999) 3564–3572, http://dx.doi.org/10.1103/PhysRevE.60.3564.

[40] C. Wagner, Theorie der alterung von niederschlägen durch umlösen (Ostwald-Reifung), Z. Elektrochem. Ber. Bunsenges. Phys. Chem. 65 (7–8) (1961) 581–591, http://dx.doi.org/10.1002/bbpc.19610650704.

[41] I.M. Lifshitz, V.V. Slyozov, The kinetics of precipitation from supersaturated solid solutions, J. Phys. Chem. Solids 19 (1–2) (1961) 35–50, http://dx.doi.org/10.1016/0022-3697(61)90054-3.

[42] Jülich Supercomputing Centre, JURECA: Data centric and booster modules implementing the modular supercomputing architecture at Jülich supercomputing centre, J. Large Scale Res. Facil. 7 (2021) A182, http://dx.doi.org/10.17815/jlsrf-7-182.